PHILOSOPHICAL TRANSACTIONS OF THE ROYAL SOCIETY A

Phil. Trans. R. Soc. A (2012) **370**, 3692–3708
doi:10.1098/rsta.2011.0201

Peak shape analysis of diagonal and off-diagonal features in the two-dimensional electronic spectra of the Fenna–Matthews–Olson complex

By Dugan Hayes and Gregory S. Engel*

Department of Chemistry and The James Franck Institute, University of Chicago, 929 East 57th St., Chicago, IL 60637, USA

We have recorded a series of two-dimensional electronic spectra of the Fenna–Matthews–Olson (FMO) complex from *Prosthecochloris aestuarii*, with several crosspeaks sufficiently resolved to permit a quantitative analysis of both the amplitude and the two-dimensional peak shape. The exponential growth and/or decay of peaks on and off the main diagonal provides information on population transfer rates between pairs of excitons. Quantum beats observed in the amplitudes and shapes of these peaks persist throughout the relaxation process, indicating that energy transfer in FMO involves both incoherent and coherent dynamics. By comparing the oscillations in the amplitude and shape of crosspeaks, we confirm theoretical predictions regarding their correlation and identify previously indistinguishable combinations of nonlinear response pathways that contribute to the signal at particular positions in the spectra. Such analysis is crucial to understanding the enormous amount of information contained in two-dimensional electronic spectra and offers a new route to uncovering a complete description of the energy transfer kinetics in photosynthetic antennae.

Keywords: nonlinear spectroscopy; photosynthesis; ultrafast; response pathways

1. Introduction

Photosynthesis comprises a multitude of intricate processes occurring in many different protein complexes, but the process starts with light harvesting in an antenna complex. The antenna consists of an array of chromophores embedded in a protein matrix; the antenna absorbs photons and transfers the resulting excitation energy towards the reaction centre, where charge separation occurs [1]. Recent work has shown that the energy transfer process in photosynthetic antennae involves both incoherent and coherent dynamics, the synergy of which enhances the transport efficiency beyond that predicted by classical theory [2,3]. This intermediate regime complicates our models of these systems but simultaneously offers the promise of inspiring highly efficient biomimetic

*Author for correspondence (gsengel@uchicago.edu).

Electronic supplementary material is available at http://dx.doi.org/10.1098/rsta.2011.0201 or via http://rsta.royalsocietypublishing.org.

One contribution of 14 to a Theo Murphy Meeting Issue ‘Quantum-coherent energy transfer: implications for biology and new energy technologies’.

technologies if we can understand and replicate the dynamics. The Fenna–Matthews–Olson (FMO) complex from green sulphur bacteria has emerged as a model system for the study of photosynthetic energy transfer due to its relative spectroscopic simplicity [4–10]. This complex contains seven non-degenerate excitonic states, a small number compared with those of most other antennae [1]. Nevertheless, these states are incompletely resolved by both linear and nonlinear absorption spectroscopies, necessitating the continued improvement of multi-dimensional techniques and the development of new analysis strategies.

Two-dimensional Fourier transform electronic spectroscopy has provided a wealth of information on the excitonic structure and dynamics of FMO and other photosynthetic antenna complexes [11]. This four-wave mixing technique probes the third-order polarization of the sample, resolving electronic couplings as off-diagonal features (crosspeaks) and providing ultrafast temporal resolution of the evolution of the electronically excited system [12–14]. Brixner *et al.* [4] presented the first two-dimensional electronic spectra of FMO and deduced excitonic couplings and energy transfer pathways from the growth of crosspeaks appearing below the main diagonal. Subsequent work by Engel *et al.* [7] identified quantum beats in the amplitudes of these crosspeaks (as well as a diagonal peak) arising from interference between the wave functions of different electronic states, indicating that electronic coherences persist in FMO throughout the energy transfer process at 77 K. Theoretical work motivated by this result demonstrated that quantum coherence can interact synergistically with environmental noise to improve the overall efficiency of energy transfer in these systems [8,9,15]. Recently, two-dimensional spectra of FMO have been used to measure electronic dephasing rates at both cryogenic and physiological temperatures, demonstrating that coherent dynamics play a role in photosynthetic energy transfer, even near 300 K [3,16]. The third-order technique has also been extended into a third Fourier dimension to separate overlapping beating signals in FMO, giving the complete set of excitonic transition energies [17].

The theoretical and experimental details of two-dimensional electronic spectroscopy have been exhaustively documented elsewhere [18–21]. Briefly, three ultrashort non-collinear laser pulses interact in the perturbative limit with the sample, inducing a third-order polarization. The signal emitted after a time t (the rephasing time) in the $\boldsymbol{k}_s = -\boldsymbol{k}_1 + \boldsymbol{k}_2 + \boldsymbol{k}_3$ phase-matching direction is heterodyne detected and spectrally resolved for a series of evenly spaced time delays τ (referred to as the coherence time) between the first and second pulses at each fixed time delay T (the waiting time) between the second and third pulses. Fourier transformation of the coherence time dimension into frequency space yields the two-dimensional frequency–frequency spectrum at the specified time T, and this process is repeated for a series of waiting times to provide temporal resolution along T. The absolute phase of the two-dimensional signal at each time T is recovered by fitting a projection of the real part of the two-dimensional signal to the separately acquired transient absorption signal, permitting separation of the signal into absorptive (real) and dispersive (imaginary) parts. The resolution of a spectrum is greatly improved by eliminating the broad dispersive component of the two-dimensional signal.

Although following the evolution of peak amplitudes in these spectra can illuminate many of the dynamics present in the system [13,22,23], much more information can be gleaned by following peak shapes as well. The information

that can be obtained from peak shapes in two-dimensional vibrational spectra has been well documented [24], but the limited resolution of two-dimensional electronic spectra has restricted the application of such analyses in the optical regime. As we will demonstrate, peak shape analysis can differentiate classes of nonlinear response pathways that are otherwise indistinguishable and can also provide information on energetic probability distributions of particular excitons and the correlations between these distributions for pairs of excitons. To quantitatively monitor the evolution of the shape of a particular peak, we assign a single scalar to the two-dimensional shape of a peak defined as the ratio of the diagonal (inhomogeneous) to the antidiagonal (homogeneous) full width at half maxima (FWHM) for each waiting time. For a diagonal peak ($\omega_\tau = \omega_t$), this aspect ratio provides information on the degree of static inhomogeneity within the ensemble [12]. The distribution of absorption and emission frequencies for a particular transition in an individual complex will be described by the same one-dimensional homogeneous probability distribution function oriented along the coherence and rephasing frequency axes, respectively, resulting in an isotropic peak. The centre frequency of this two-dimensional function will vary between complexes within the ensemble owing to small structural differences that result in relative solvatochromic shifts, and the peak observed for the ensemble will be the sum of the individual isotropic peaks distributed along the diagonal. The diagonal ellipticity of a diagonal peak therefore provides a direct measure of the relative magnitudes of the different broadening mechanisms present in the sample.

The only diagonal feature that is individually resolved in a two-dimensional spectrum of FMO beyond the first 100 fs of waiting time is the peak corresponding to the lowest energy exciton [5,23,25]. The other six closely spaced transitions overlap such that only a single diagonally elongated peak is observed after the first few hundred femtoseconds, thereby precluding the measurement of individual linewidths. This problem could be addressed by measuring the linewidths of crosspeaks, but despite being separated into a second dimension, the off-diagonal features observed in the previously reported two-dimensional spectra of FMO from *Chlorobaculum tepidum* are still not sufficiently resolved to permit such measurements [16].

Here, we present a series of two-dimensional electronic spectra of FMO isolated from *Prosthecochloris aestuarii* showing several crosspeaks suitably well resolved to permit peak shape analysis. The diagonal and antidiagonal linewidths of a crosspeak are not, however, directly related to the inhomogeneous and homogeneous broadening of a particular transition, as is true for a diagonal peak. Instead, the diagonal ellipticity of a crosspeak provides a measure of the degree to which the transition energy distributions of the two excitons that give rise to the peak are correlated [26–28]. Because the coherence and rephasing frequencies of a crosspeak are non-degenerate, the frequency distributions along the two axes will be described by different one-dimensional distribution functions. If these distributions are uncorrelated, then we observe a peak that is symmetric along both dimensions (the peak will not necessarily be isotropic, however, as the linewidths of the two transitions are independent). Elongation of a crosspeak along the diagonal, on the other hand, indicates that the distributions are positively correlated, meaning that the same set of microscopic configurations yields hypsochromic or bathochromic shifts in the transition energies of both excitons.

Such correlations are necessary for electronic coherences to survive in a dynamic, disordered environment. Uncorrelated fluctuations in individual exciton transition energies subsequently introduce fluctuations in the difference frequencies of corresponding interexcitonic coherences, resulting in the dephasing of these coherences as they evolve [16]. Previous studies have suggested that the protein scaffold of photosynthetic antennae and reaction centres is the source of these correlations, introducing global fluctuations that promote energy transfer without dephasing coherences [29]. Long-lived electronic coherence in antenna complexes has also been implicated in the enhancement of transport efficiency beyond the classical, incoherent limit [7]. We find that three different crosspeaks in the two-dimensional spectra of FMO remain diagonally elongated beyond the first picoseconds of waiting time, demonstrating that the transition energy fluctuations of the respective pairs of excitons are positively correlated. This finding is in agreement with the long-lived quantum beating also observed in the amplitudes and shapes of these peaks.

2. Third-order response pathways

This section serves as an explanation and summary of the different nonlinear response pathways that contribute to the full third-order polarization of the sample in a two-dimensional experiment. These pathways arise from the density matrix formalism, which provides a statistical description of the time dependence of the ensemble interacting with the radiation field. The time evolution of the density operator ρ is given by the Liouville–von Neumann equation,

$$\dot{\rho}(t) = -\frac{\mathrm{i}}{\hbar}[H(t), \rho(t)]. \tag{2.1}$$

Separating H into a system Hamiltonian H_0 and a perturbative interaction H_{int} and performing an expansion on ρ gives

$$\dot{\rho}^{(n)}(t) = -\frac{\mathrm{i}}{\hbar}([H_0(t), \rho^{(n)}(t)] + [H_{\mathrm{int}}(t), \rho^{(n-1)}(t)]), \tag{2.2}$$

which can be iteratively integrated from $\rho^{(0)}$ to give an expression for $\rho^{(3)}$ with a total of 48 terms called Liouville (or response) pathways [12]. Finally, the third-order polarization can be calculated from the third-order density operator and the dipole operator V according to

$$P^{(3)} = \mathrm{Tr}[V\rho^{(3)}]. \tag{2.3}$$

The number of response pathways detected in a two-dimensional experiment is reduced from 48 to 16 by experimentally controlling the order of interactions and requiring the third interaction to be with $\boldsymbol{k}_3$. We further reduce the number of pathways to six by detecting only in the $\boldsymbol{k}_s = -\boldsymbol{k}_1 + \boldsymbol{k}_2 + \boldsymbol{k}_3$ phase-matching direction. These remaining pathways are represented graphically using double-sided Feynman diagrams in figure 1*a–f*. In these diagrams, an interaction with the ket of the density operator is depicted by a curved arrow pointed towards (absorption) or away from (stimulated emission, SE) the left vertical line, whereas the same interactions with the bra are depicted by an arrow acting on the right vertical line. The ground state of the system is given by $|g\rangle$, one-exciton states

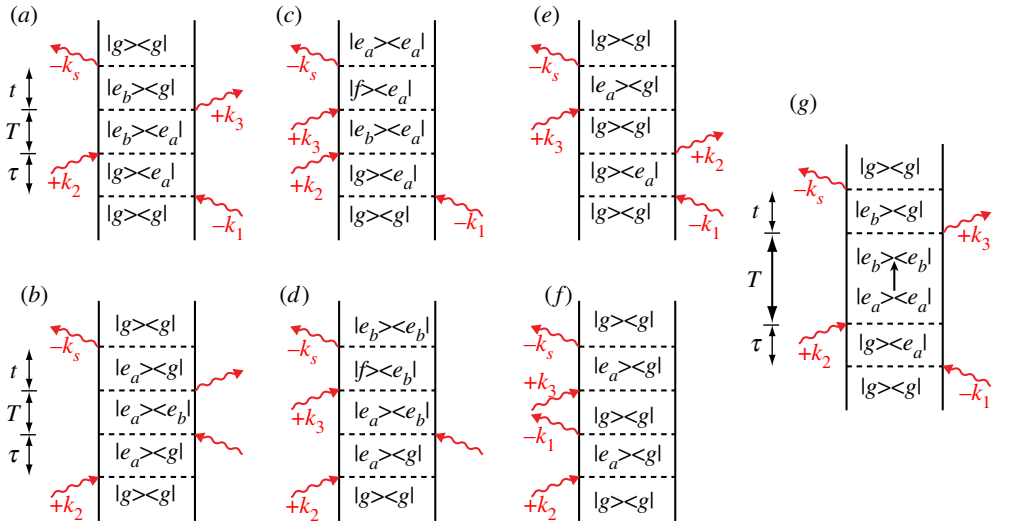

Figure 1. Double-sided Feynman diagrams representing the types of nonlinear response pathways contributing to the signal in a standard two-dimensional experiment. An interaction with the ket of the density operator is depicted by a curved arrow pointed towards (absorption) or away from (stimulated emission, SE) the left vertical line, while the same interactions with the bra are depicted by an arrow acting on the right vertical line. The ground state of the system is given by $|g\rangle$, one-exciton states are given by $|e_j\rangle$, and a two-exciton state is given by $|f\rangle$. Time progresses upwards, and the delays τ, T and t are indicated to the left. Diagrams (a) and (b) correspond to SE, diagrams (c) and (d) to excited state absorption (ESA), and diagrams (e) and (f) to ground state bleaching (GSB). Diagram (g) illustrates population transfer during the waiting time for a stimulated emission pathway. The pathways shown in diagrams (a), (c) and (e) result in a rephasing (photon echo) signal, while those in diagrams (b), (d) and (f) result in a non-rephasing free induction decay. (Online version in colour.)

are given by $|e_j\rangle$ and a two-exciton state is given by $|f\rangle$. Time progresses upwards, and the delays τ, T and t are indicated to the left. Diagram (g) illustrates population transfer during the waiting time for one of the six response pathways. The sign of the signal corresponding to a particular diagram is given by $(-1)^m$, where m is the number of interactions on the right. Diagrams (a) and (b), which correspond to SE pathways, and diagrams (e) and (f), which correspond to ground state bleach (GSB) pathways, produce a positive signal. Diagrams (c) and (d), which correspond to excited state absorption (ESA) pathways, produce a negative signal.

After the first interaction, the system is in a single-quantum coherence and evolves phase at the optical frequency ω_{ag} (figure 1a,c,e) or $\omega_{ga} = -\omega_{ag}$ (figure 1b,d,f) during the coherence time. The second interaction puts the system in a stationary population state or a zero-quantum coherence that evolves phase at the difference frequency ω_{ab} or ω_{ba} during the waiting time. Finally, the third interaction returns the system to a single-quantum coherence that evolves phase during the coherence time in either the opposite (figure 1a,c,e) or the same (figure 1b,d,f) direction as it did during the coherence time before emitting the signal pulse. Because the system evolves phase in opposite directions during τ and

t in the top diagrams, it is said to rephase. Any inhomogeneous dephasing that occurs during τ is eliminated as the ensemble rephases during t, resulting in a macroscopic repolarization and emission of a photon echo [12]. On the other hand, the bottom diagrams correspond to non-rephasing pathways, which continue to dephase during t and emit a weaker free induction decay signal.

The non-collinear beam geometry in our optical setup permits separation of the signals from rephasing and non-rephasing pathways simply by controlling the order of the first two interactions. In the experimental phase-matching direction, rephasing pathways correspond to interaction with $\boldsymbol{k}_1$ before $\boldsymbol{k}_2$, whereas the order is reversed for non-rephasing pathways. The signals can be analysed separately (to give rephasing and non-rephasing spectra) or together (to give a combined (or total) spectrum). The combined, rephasing and non-rephasing spectra of FMO at $T = 500$ fs are shown in the electronic supplementary material, figure S1, illustrating the different peak shapes associated with each type of spectrum. The elimination of inhomogeneous dephasing in rephasing pathways results in peaks that are elongated along the main diagonal, while non-rephasing peaks are inhomogeneously broadened in the direction perpendicular to the main diagonal.

3. Experimental methods

The FMO sample was isolated from *P. aestuarii* as described previously [30] and solubilized in 800 mM tris/HCl buffer (pH 8.0) with 0.1 per cent lauryldimethylamine oxide detergent. This solution was mixed with glycerol 35 : 65 (v/v) and loaded into a quartz cell with a path length of 200 µm (Starna). The cell was cooled in a cryostat (Oxford Instruments) to 77 K. The optical density of the sample at 809 nm was measured to be 0.30.

In our spectroscopic setup, the output of a self-mode-locking Ti : sapphire oscillator (Coherent Micra) was used to seed a regenerative amplifier (Coherent Legend Elite) to produce a 5.0 kHz pulse train of 38 fs pulses centred at 809 nm with a spectral bandwidth of 34 nm (FWHM). The 10 Hz stability of the laser was measured to be 0.15 per cent (s.d./mean) over the course of the experiment. The beam was split with a 50 : 50 beam splitter (CVI Melles Griot), and a time delay (the waiting time T) and vertical offset were introduced between the beams using a retroreflector mounted on a motorized translation stage (Aerotech). The beams were focused onto a diffractive optic (HoloEye), giving two pairs of phase-locked beams arranged in a box geometry. Another time delay (the coherence time τ) was introduced between one pair of beams by sending each through a pair of 1° fused silica wedges (Almaz Optics) mounted on motorized translation stages (Aerotech). The local oscillator (LO) beam was attenuated using absorptive neutral density filters with a total optical density of 3.1 at 809 nm. All beams were focused to a spot size approximately 70 µm in diameter in the sample, where the total incident power was 3.3 nJ (1.1 nJ per pulse). The LO was aligned into a 0.3 m spectrometer (Andor Shamrock) and focused on a 1600 × 5 pixel region centred on a back-illuminated charge-coupled device (Andor Newton) thermoelectrically cooled to −50°C. Calibration of the delay stages was performed as reported previously using spectral interferometry [20,31].

Spectra were acquired by stepping the coherence time from −300 to 600 fs in steps of 4 fs for each fixed waiting time. The waiting time was scanned from 0 to 1200 fs in steps of 20 fs, and multiple spectra at $T = 0$ were taken throughout the data acquisition to monitor sample integrity. No indication of photodamage was observed. Spectra were also acquired at $T = 2$, 5, 10, 20 and 50 ps. Scatter subtraction, Fourier windowing and transformation to frequency–frequency space were performed as reported elsewhere [20]. The pump-probe signal was also acquired at each waiting time to recover the absolute phase of the two-dimensional spectra and separate the third-order signal into absorptive (real) and dispersive (imaginary) parts. For each time T, the transient absorption signal was recorded 100 times over 140 s, and the average signal was fit to the projection of the real part of the two-dimensional signal along the coherence dimension, as reported elsewhere [20].

Amplitude traces were taken from the series of two-dimensional spectra by integrating over a circle with a radius of $10\,\mathrm{cm}^{-1}$ centred at the coordinates of the peak under consideration. Because these traces exhibit exponential growth and/or decay owing to population relaxation (see figure 1*g*), each was fitted to the sum of two exponential terms. The fits were subtracted from the traces to facilitate comparison with the peak shape traces, which are unaffected by incoherent dynamics. The diagonal linewidth of a peak at $(\omega_\tau = \omega_a, \omega_t = \omega_b)$ at a given waiting time was determined by cutting through that point along the line parallel to the main diagonal according to $\omega_t = \omega_\tau + (\omega_b - \omega_a)$ and fitting the vector of points within $50\,\mathrm{cm}^{-1}$ of the peak to a single Gaussian function. The antidiagonal linewidth was similarly determined by cutting along the line orthogonal to the main diagonal according to $\omega_t = -\omega_\tau + (\omega_a + \omega_b)$. The peak shape was reported as the quotient of these two linewidths.

4. Results and discussion

A series of two-dimensional spectra of FMO taken at increasing values of T is shown in figure 2, where we present the real (absorptive) part of the signal from both rephasing and non-rephasing response pathways. Each two-dimensional spectrum has been normalized to its respective maximum. The time evolution of the spectrum agrees well with the experimental and theoretical results of Read *et al.* [23]. Within the first hundred femtoseconds, the diagonal peaks corresponding to excitons 1, 2 and 4 are resolved at 12 120, 12 285 and 12 440 cm^{-1}, respectively. The only clear off-diagonal features observed at this time are a broad ESA band above the diagonal and a positive band below the diagonal corresponding to emission at the exciton 2 frequency. Owing to the proximity of this latter feature to the stronger main diagonal peak, it is unclear whether this band contains contributions from both the 3–2 $(\omega_\tau = 12\,400\,\mathrm{cm}^{-1}, \omega_t = 12\,285\,\mathrm{cm}^{-1})$ and 4–2 $(\omega_\tau = 12\,440\,\mathrm{cm}^{-1}, \omega_t = 12,285\,\mathrm{cm}^{-1})$ crosspeaks or is simply the incompletely resolved 4–2 crosspeak. According to the calculations of Read *et al.*, excitons 2 and 4 bear the greatest transition dipole magnitudes, while the dipoles of excitons 3 and 4 are most closely parallel to that of exciton 2. The 3–2 crosspeak and especially the 4–2 crosspeak are therefore expected to dominate at early waiting times. Other minor distortions are evident near the 1–2 and 2–1 crosspeak coordinates ($\omega_\tau = 12\,120, \omega_t = 12\,285$ and $\omega_\tau = 12\,285$,

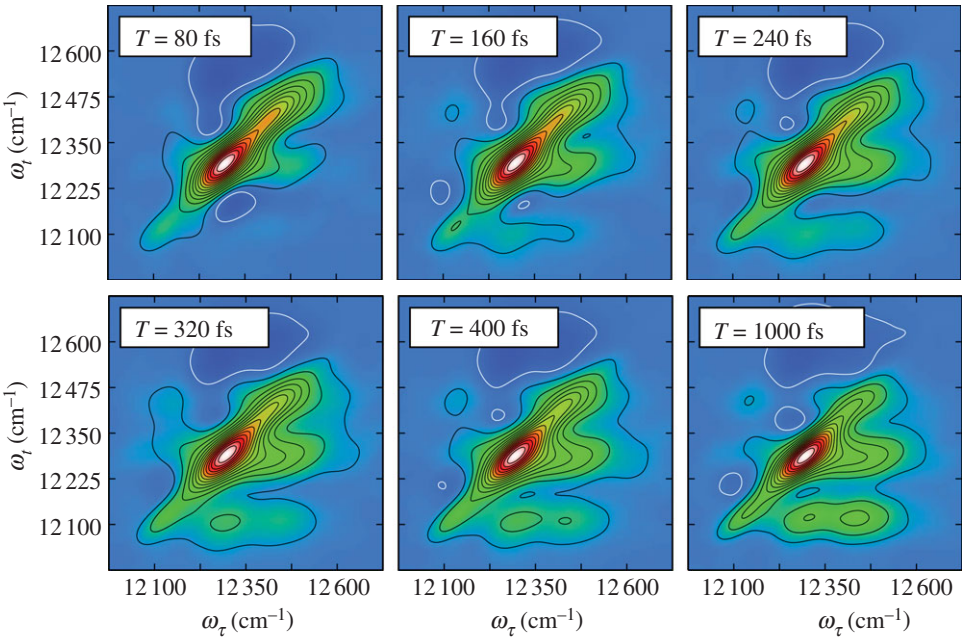

Figure 2. A series of two-dimensional spectra of FMO taken at increasing values of T. These spectra contain the real (absorptive) part of the signal from both rephasing and non-rephasing response pathways. The colour and contours lines are scaled linearly. Black contour lines correspond to positive features and white contour lines to negative features. (Online version in colour.)

$\omega_t = 12\,120\,\mathrm{cm}^{-1}$, respectively), but these features are still too weak to separate from the main diagonal. The lack of strong crosspeaks at $T = 80$ fs indicates that the mutual cancellation of the signals from the ESA, SE and GSB pathways at most off-diagonal positions is nearly complete.

At later waiting times, the exciton 4 diagonal peak decays, while the 4–2 crosspeak intensifies. As discussed by Read *et al.*, this behaviour can be attributed to relaxation from exciton 4 to 2, with the 4–2 crosspeak reaching a maximum amplitude within 400 fs. Our spectra also clearly reveal relaxation from exciton 4 to 1, but the growth of the 4–1 crosspeak occurs at a significantly slower rate, not reaching a maximum until nearly 2 ps. This growth is accompanied by the slow decay of the 4–2 crosspeak, indicating that relaxation occurs directly from exciton 4 to 2, but only indirectly from exciton 4 to 1 via exciton 2. This result is in accordance with the theoretical transfer pathways calculated by Read *et al.* The direct relaxation from exciton 2 to 1 is evident from the appearance of the 2–1 crosspeak, which effectively plateaus within 700 fs.

The amplitudes of the 1–4 and 1–2 crosspeaks, on the other hand, remain relatively static. Although these peaks (and the exciton 1 diagonal peak) appear to grow slightly within the first 300 fs in figure 2, this occurs only because each spectrum is normalized to its respective maximum (the exciton 2 diagonal peak), which decays on a similar time scale. Because population transfer is not thermodynamically favourable from exciton 1 to either 2 or 4, these peaks are not expected to—and indeed do not—exhibit exponential growth. Instead, these

peaks gradually decay as the coherences between excitons 1 and 2 and excitons 1 and 4, which give rise to the rephasing SE signal at these coordinates (see figure 1*a*), dephase. We confirm our earlier-mentioned conclusions by comparing the amplitudes of crosspeaks at conjugate positions at early waiting times. The 1–2 crosspeak is not well separated from the main diagonal, but a comparison of the 1–4 and 4–1 crosspeaks shows that the amplitudes are nearly equal for the first 200 fs until population relaxation begins to dominate and the 4–1 crosspeak begins to grow exponentially. The amplitude traces of the exciton 1 diagonal peak and the 4–1, 2–1 and 2–6 crosspeaks, taken from the combined, rephasing and non-rephasing spectra, are plotted in the electronic supplementary material, figure S2. A thorough quantitative description of the kinetics of this system will be the subject of a future publication.

Beyond the previously discussed population transfer dynamics, the improved resolution of the off-diagonal features in these two-dimensional spectra also permits a detailed analysis of coherent dynamics in FMO. The resolution enhancement in these spectra compared with those published previously appears primarily along the red edge in both spectral dimensions and is therefore attributed to a difference in laser bandwidth. The FWHM of the laser pulse used in the present work spans from 792 to 826 nm, extending 5.5 nm beyond the red edge of the pulse used in the previous experiment and reaching the transition of the lowest energy exciton (825 nm). For the first time, we are able to quantitatively follow the evolution of the shape of individual peaks, both on and off the main diagonal and compare quantum beating signatures in these traces to those in the corresponding peak amplitude traces. Figure 3*a* shows an overlay of the amplitude (solid line) and shape (dashed line) of the exciton 1 diagonal peak as a function of waiting time. The amplitude was fit to the sum of two exponential decays, and this fit was subtracted to give the residual amplitude plotted in figure 3 in order to facilitate comparison with the peak shape trace. The complex beating signature in both traces arises primarily from the non-rephasing SE response pathways (figure 1*b*) in which the system is in a coherence between exciton 1 and any of the higher energy states during the waiting time. In agreement with theoretical predictions, the shape and amplitude beats of this diagonal peak are clearly anticorrelated [28].

This behaviour was previously observed in the exciton 1 diagonal peak of FMO isolated from *C. tepidum* [7]. While the FMO complexes from *C. tepidum* and *P. aestuarii* bear a striking similarity in crystal structure, clear differences in the excitonic structures are apparent, even in the linear absorption spectra. Indeed, the beating pattern observed here is quite different from the pattern observed in the *C. tepidum* spectra; as expected, only the anticorrelation between peak shape and amplitude is shared by both complexes. The origin of this anticorrelation can be understood through a consideration of the Feynman diagrams that contribute to the signal on the diagonal in the experimental phase-matching condition [14]. For simplicity, we will not consider relaxation during waiting time, but only the unitary evolution of the elements of the density matrix. The signal from the rephasing response pathways represented by diagram (*a*) will appear on the diagonal only when $a = b$. Consequently, the system will be in a population during the waiting time for these pathways, and the signal will only exhibit incoherent (exponential) evolution. On the other hand, the signal from the non-rephasing pathways represented by diagram B will appear on the diagonal, irrespective of

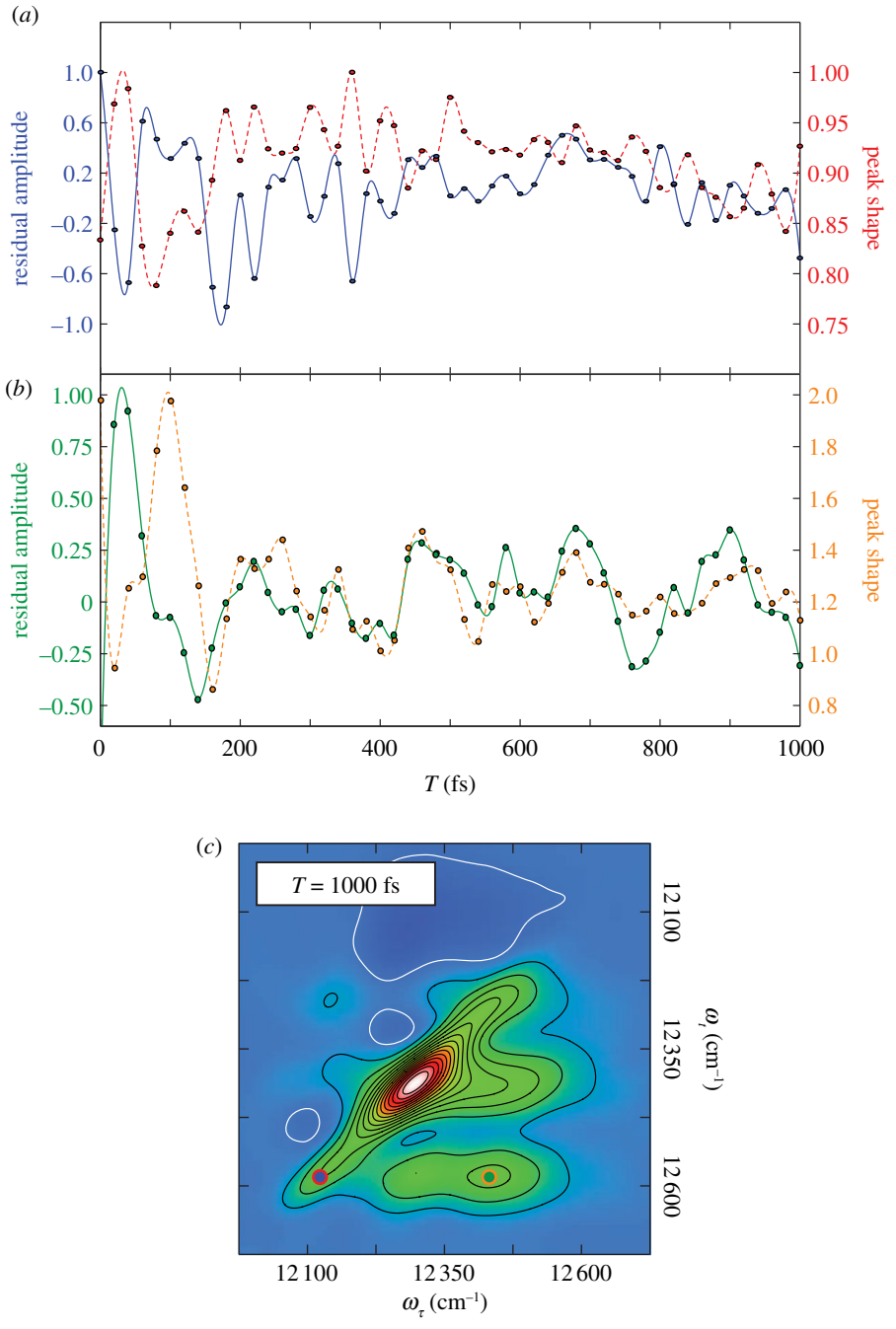

Figure 3. Characteristic anticorrelation and correlation of peak shapes and amplitudes on and off the main diagonal. (*a*) The residual amplitude (solid line) and shape (dashed line) of the exciton 1 diagonal peak are overlain as a function of waiting time. The vectors were interpolated using a cubic spline function, and the data points are shown as black circles. (*b*) The same traces (solid and dashed lines, respectively) for the 4–1 crosspeak, and the locations of the two peaks in the two-dimensional spectrum are indicated in (*c*). (Online version in colour.)

the identity of state $|e_b\rangle$. When $a \neq b$, the unitary evolution of the quantum coherence during the waiting time results in the periodic modulation of the non-rephasing signal amplitude at the difference frequency $\omega_{ab} = (\varepsilon_a - \varepsilon_b)/\hbar$. As discussed earlier, the elimination of inhomogeneous dephasing in rephasing signals (photon echoes) results in diagonally elongated peaks, while the inhomogeneous dephasing in non-rephasing signals (free induction decays) results in round peaks with significantly broader antidiagonal linewidths. A diagonal feature will therefore contain contributions from a diagonally broad, static peak and several round peaks that exhibit amplitude oscillations. Consequently, the amplitude of a diagonal peak will reach a local maximum when the peak is narrow along the diagonal and broad along the antidiagonal, or in other words, the two-dimensional peak shape is at a local minimum.

Figure 3*b*, however, illustrates the opposite behaviour in the 4–1 crosspeak: the residual amplitude (solid line) and shape (dashed line) of this peak exhibit correlated oscillations after the first 140 fs (because the peak is not resolved in the spectrum at early times, the peak shape measurements before 140 fs are unreliable). This correlation is also theoretically expected, although quantitative analysis of the shape of electronic crosspeaks has not been possible with previously reported spectra owing to incomplete resolution of off-diagonal features. Here, we experimentally verify the theoretical prediction, complementing the work on diagonal peak shapes performed previously [7].

We again turn to the Feynman diagrams in figure 1 to understand this phenomenon. The rephasing SE pathways (figure 1*a*) will contribute to a crosspeak only when $a \neq b$, meaning the system will be in a quantum coherence during the waiting time and beat at the difference frequency ω_{ab}. The signal from any rephasing ESA pathways (figure 1*c*) will appear off the main diagonal (excluding accidental degeneracies between the one- and two-exciton manifolds), but the signal from these pathways will only beat when $a \neq b$. Meanwhile, no non-rephasing SE pathways (figure 1*b*) contribute to signal off the main diagonal in the experimental phase-matching direction; as discussed earlier, the signal from figure 1*b* will always appear on the diagonal. There are off-diagonal non-rephasing ESA pathways (figure 1*d*, $a = b$) and GSB pathways (figure 1*f*, $a \neq b$), but the signal from these pathways does not beat during the waiting time. Accordingly, the oscillatory evolution of the crosspeak arises exclusively from the rephasing pathways [14]. Unlike the simpler diagonal case, the relation between the amplitude and peak shape for a crosspeak will depend upon the type of (rephasing) response pathway responsible for the quantum beats. For an SE pathway, the amplitude and diagonal linewidth will beat together, while the antidiagonal linewidth beats out of phase, resulting in correlation between the amplitude and shape. The negative sign before the amplitude for an ESA pathway, on the other hand, results in anticorrelation.

Although the rephasing SE and ESA pathways beat out of phase with each other, the ESA signal is red-shifted along the rephasing frequency axis by the binding energy of the biexciton state $|f\rangle$ and does not overlap perfectly with the SE crosspeak [32]. The destructive interference between the two signals will be incomplete, but such interference can still impede the accurate measurement of the shape and amplitude of a crosspeak when the binding energy is not sufficiently greater than the linewidths of the excitations. Nevertheless, figure 3 demonstrates that this is not always the case, and the complex behaviour of

crosspeak beats highlights another potential application of off-diagonal peak shape analysis. The amplitude beating in a negative crosspeak could arise from a rephasing ESA pathway or from a rephasing SE pathway that appears at the same position as a strong static rephasing (figure 1*c*, $a = b$) or a non-rephasing ESA signal. Eliminating the third possibility (rephasing SE + non-rephasing ESA) is as simple as removing the non-rephasing signal from the spectra by taking only the data points for which $\tau > 0$ when transforming the coherence dimension from time to frequency space (see the electronic supplementary material, figure S1). The other two possibilities, however, involve only rephasing pathways and are indistinguishable unless the peak shape and amplitude oscillations are compared. The first case (rephasing ESA, $a \neq b$) results in anticorrelation, while the second case (rephasing SE + rephasing ESA, $a = b$) results in correlation. We observe correlated beating in the shape and amplitude of the negative 2–6 crosspeak ($\omega_\tau = 12\,285$, $\omega_t = 12\,560\,\mathrm{cm}^{-1}$, see the electronic supplementary material, figure S3), and thus we conclude that this signal arises from the sum of rephasing SE and ESA ($a = b$) pathways.

A close inspection of the behaviour of a different off-diagonal feature, the 2–1 crosspeak, illustrates the different factors that give rise to the correlated peak shape and amplitude beating. Figure 4*a* shows the section of the total two-dimensional spectrum of FMO corresponding to the 2–1 crosspeak (horizontal dimensions) as it evolves in waiting time (vertical dimension). The three-dimensional spectrum is scaled linearly in both colour and opacity to prevent obfuscation of the centre of the two-dimensional slices. As shown before in figure 2, the 2–1 crosspeak appears within the first 100 fs and continues to grow for the next 600 fs. Periodic oscillations in the amplitude of the peak are clearly visible by looking down the (T, ω_t) plane along the ω_τ-axis. This view also shows that the diagonal linewidth (which, in this orientation, corresponds to the horizontal cut through the (ω_τ, ω_t)-plane) is maximized at the same times T as the peak amplitude. Meanwhile, the view down the (T, ω_τ)-plane along the ω_t-axis shows that the antidiagonal linewidth (which corresponds to the vertical cut through the (ω_τ, ω_t)-plane) is maximized at the times T that fall between successive amplitude maxima. The periodic diagonal elongation of the peak is highlighted in figure 4*d*, where the waiting times presented correspond to successive peak shape extrema.

The peak shape (dashed line) and residual amplitude (solid line) are plotted in figure 4*b*,*c*, respectively, again showing correlation between the two beating signals, as previously shown with the 4–1 crosspeak in figure 3. Despite the additional analysis necessary to calculate the two-dimensional peak shape, this property appears to be more robust to noise than the peak amplitude. It would be advantageous, then, to use peak shape traces instead of amplitude traces when performing Fourier analysis of oscillatory features in two-dimensional spectra, although this approach is possible only when the peak of interest is well resolved.

Recent work by Christensson *et al.* [33] has shown that the anticorrelation between diagonal peak shape and amplitude beats is a signature of any quantum coherence and not exclusively electronic coherences, as previously assumed. However, we have recently reported results from isotopic substitution experiments that confirm earlier claims that the beating signals found in the two-dimensional electronic spectra of FMO arise from electronic, and not vibrational, coherences [34]. The data from those experiments show that the random partial deuteration

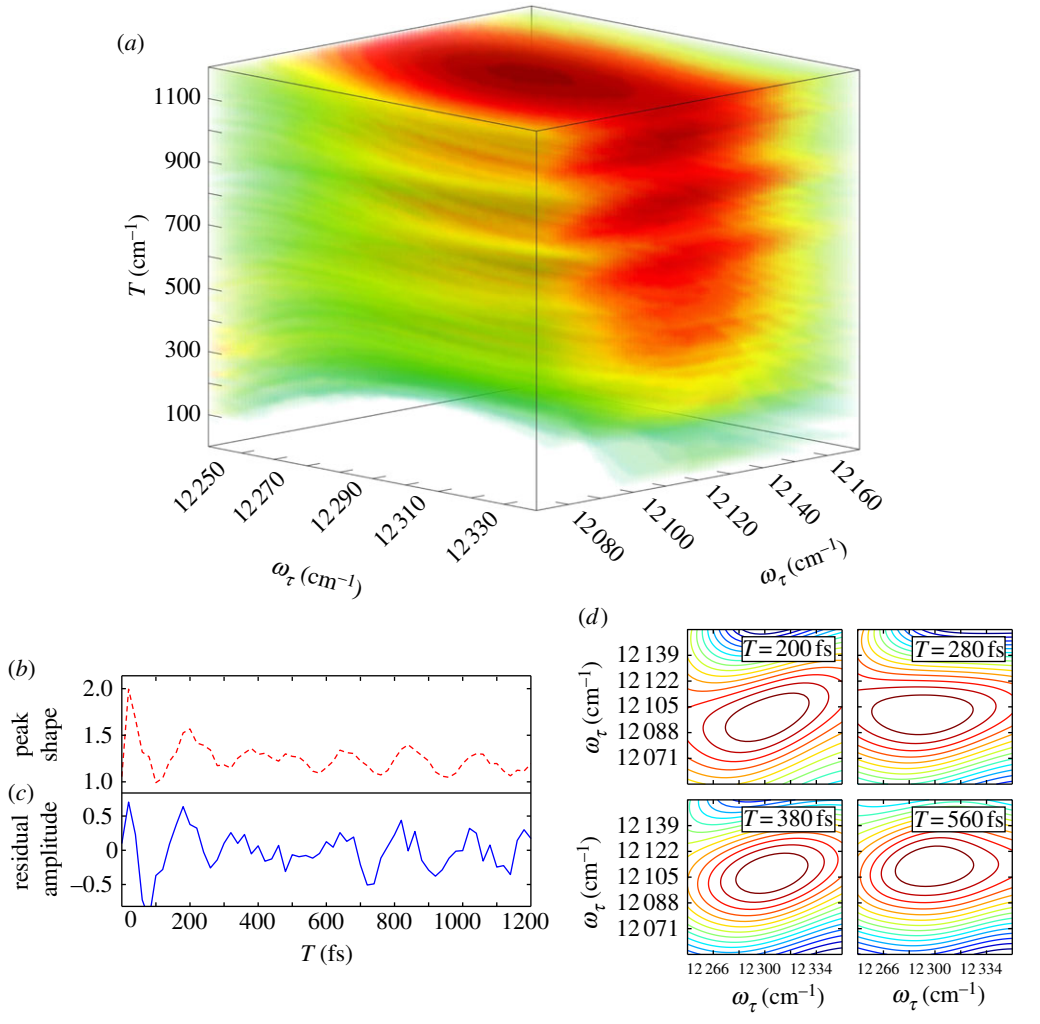

Figure 4. A detailed analysis of the evolution of the 2–1 crosspeak. (*a*) Section of the total two-dimensional spectrum of FMO corresponding to this peak (horizontal dimensions) as it evolves in waiting time (vertical dimension). The three-dimensional spectrum is scaled linearly in both colour and opacity to prevent obfuscation of the centre of the two-dimensional slices. (*b*,*c*) The peak shape (dashed line) and residual amplitude (solid line) are plotted, respectively, and (*d*) linearly scaled contour plots of the peak. (Online version in colour.)

of FMO from *C. tepidum*, which necessarily introduces further inhomogeneity in the vibrational but not electronic modes of the chromophores, does not affect the dephasing rate of individual beating signals. Furthermore, we have separated the amplitude traces into rephasing and non-rephasing components (see the electronic supplementary material, figure S2), and found that the beating observed in the crosspeaks appears only in the rephasing signals, a signature of electronic coherence [35]. Therefore, while we cannot use the peak shape analysis to distinguish between electronic and vibrational coherences, we can use it to characterize the dephasing of beating signals that have been otherwise identified

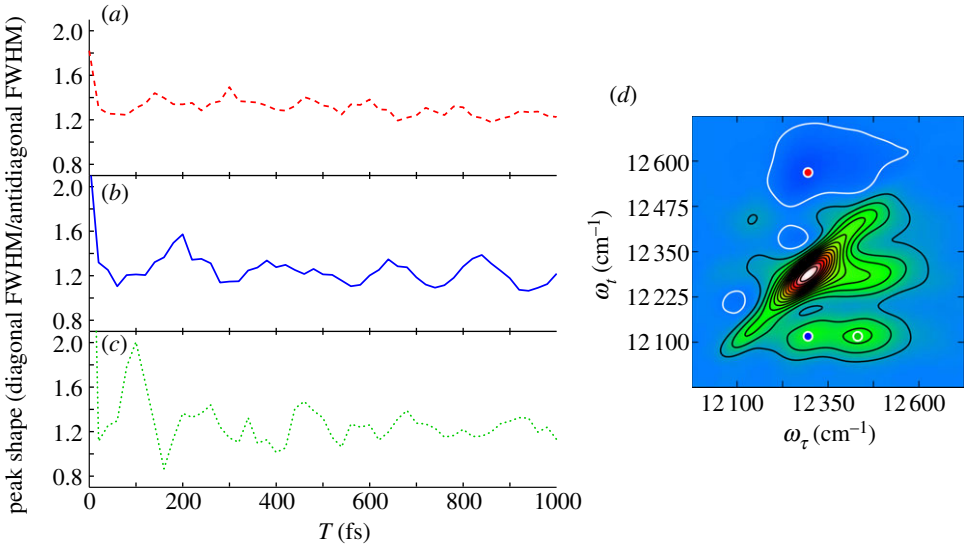

Figure 5. (*a–c*) The peak shape traces of the 2–6 (top, dashed line), 2–1 (middle, solid line), and 4–1 (bottom, dotted line) crosspeaks, respectively. (*d*) The locations of these peaks in the two-dimensional spectrum are indicated. (Online version in colour.)

as arising from electronic coherences. The determination of electronic dephasing rates in FMO has been previously accomplished by fitting damped oscillations to the evolution of crosspeak amplitudes [16], but as shown in figure 4, fitting to the evolution of the peak shape would be preferable when possible, owing to the robustness of this measurement to noise.

The beating signatures seen in both the peak shape and amplitude traces indicate that the coherences that give rise to these beats persist well beyond the first picoseconds of waiting time. A consideration of the amplitudes of the peak shape beats and the final values to which the traces converge offers further insights into the dynamics of the system and demonstrates the mechanism by which these coherences survive. The peak shape traces of the 4–1, 2–1, and 2–6 crosspeaks are shown in figure 5, demonstrating that this analysis is possible for both positive and negative crosspeaks. Because these features are not fully resolved within the first 140 fs, the traces are not reliable at early times, but the oscillations in the peak shapes after 140 fs demonstrate striking similarities. Although the difference frequencies—and, consequently, the beating frequencies—associated with the three crosspeaks are distinct, the first local maximum of each trace appears at a value of approximately 1.5, and each trace eventually approaches a final value of approximately 1.2. Even at $T = 5$ ps, the 2–1 crosspeak, for example, remains diagonally elongated, with a peak shape of 1.18. At much later times, however, this crosspeak becomes essentially symmetric about both frequency dimensions, with a peak shape of 1.07 at $T = 10$ ps, 1.03 at $T = 20$ ps and 0.98 at $T = 50$ ps. The persistence of diagonal ellipticity (peak shape > 1) beyond $T = 1$ ps in each of the crosspeaks demonstrates positive correlation between the energy fluctuations of the corresponding pairs of excitons, as explained previously [26,27]. An environmental fluctuation such as a local protein motion that causes, for instance, a bathochromic (hypsochromic) shift in

the transition frequency of exciton 4 also causes a bathochromic (hypsochromic) shift in the transition frequencies of excitons 1 and 2, and accordingly, excitation at the red (blue) edge of exciton 4 is correlated with emission at the red (blue) edge of exciton 1 or 2. As a result, the difference frequencies of the 2–1 and 4–1 coherences are relatively constant within the first few picoseconds, preventing the zero-quantum coherences from dephasing on the same time scale as the corresponding one-quantum coherences [29]. These correlations approach zero within 10 ps, however, indicating that sources of fluctuations on this time scale, such as larger protein motions, eventually dephase the coherences.

Although the values of the maxima of each of the crosspeak shape traces are comparable, the minima clearly are not. Each trace is plotted on the same vertical scale, and consequently the beating of the 2–6 peak shape is more difficult to discern, as the differences between successive maxima and minima are significantly less than they are for the other two traces: while the shapes of the 2–1 and 4–1 crosspeaks approach unity, the shape of the 2–6 crosspeak never drops below 1.2 in the first ps. The fact that the 2–6 crosspeak remains somewhat diagonally elongated at all times T indicates that non-rephasing ESA pathways do not contribute to this negative feature; otherwise, the peak shape would approach unity at the times corresponding to the local minima of the rephasing signal. This is easily confirmed by an examination of the non-rephasing trace in the electronic supplementary material, figure S2, which does not show a negative feature at this position. As explained earlier, this feature corresponds to the sum of rephasing SE and ESA ($a = b$) signals (see the electronic supplementary material, figure S3).

Finally, we note that the beats observed in the peak shape traces do not dephase significantly within this 1 ps window. As illustrated by figures 2 and 4, the majority of the signal at the crosspeaks below the main diagonal after the first 200 fs can be ascribed to population relaxation from higher energy states, but the peak shape (and amplitude) beats persist as relaxation progresses. Because the incoherent relaxation process does not destroy the coherences within the system as it redistributes the excitation energy, we conclude that the overall energy transfer mechanism must also include environment-induced coherence transfer processes in the spirit of previous studies of FMO from *C. tepidum* [7].

5. Conclusion

The improved resolution in the two-dimensional electronic spectra of FMO from *P. aestuarii* over the spectra of FMO from *C. tepidum* has allowed us to explore new analysis strategies that before were only possible in theory. We have measured the amplitudes and shapes of four different fully resolved peaks both negative and positive, both on and off the main diagonal. Not only do the results from our measurements confirm theoretical predictions of the behaviour of quantum beats in these different features, but they also have enabled us to begin to dissect the complex array of nonlinear response pathways that sum to give the total two-dimensional spectrum. The persistence of the diagonal elongation of crosspeaks at long waiting times ($T > 1$ ps) demonstrates correlation between exciton transition energy distributions, providing insights into both the electronic structure of the complex and the mechanism by which electronic coherences

survive in a disordered environment. Similar analyses will be invaluable in the continuing efforts towards understanding the complete dynamics of energy transfer in biological systems.

We acknowledge the experimental efforts of Kelly A. Fransted and Gitt Panitchayangkoon in collecting this data, and we thank Jianzhong Wen and Robert E. Blankenship for providing the FMO sample. The authors declare no conflict of interest. This work was supported in part by grant nos HR0011-09-1-0051 and N66001-10-1-4060 from the Defense Advanced Research Projects Agency and grant no. FA9550-09-1-0117 from the Air Force Office of Scientific Research as well as funding from the Dreyfus Foundation and the Searle Foundation. D.H. is supported in part by the NSF GRF programme.

References

1 Blankenship, R. E. 2002 *Molecular mechanisms of photosynthesis*. Malden, MA: Blackwell Science.
2 Collini, E., Wong, C. Y., Wilk, K. E., Curmi, P. M. G., Brumer, P. & Scholes, G. D. 2010 Coherently wired light-harvesting in photosynthetic marine algae at ambient temperature. *Nature* **463**, 644–647. (doi:10.1038/nature08811)
3 Panitchayangkoon, G., Hayes, D., Fransted, K. A., Caram, J. R., Harel, E., Wen, J., Blankenship, R. E. & Engel, G. S. 2010 Long-lived quantum coherence in photosynthetic complexes at physiological temperature. *Proc. Natl Acad. Sci. USA* **107**, 12 766–12 770. (doi:10.1073/pnas.1005484107)
4 Brixner, T., Stenger, J., Vaswani, H. M., Cho, M., Blankenship, R. E. & Fleming, G. R. 2005 Two-dimensional spectroscopy of electronic couplings in photosynthesis. *Nature* **434**, 625–628. (doi:10.1038/nature03429)
5 Cho, M. H., Vaswani, H. M., Brixner, T., Stenger, J. & Fleming, G. R. 2005 Exciton analysis in 2D electronic spectroscopy. *J. Phys. Chem. B* **109**, 10 542–10 556. (doi:10.1021/jp050788d)
6 Adolphs, J. & Renger, T. 2006 How proteins trigger excitation energy transfer in the FMO complex of green sulfur bacteria. *Biophys. J.* **91**, 2778–2797. (doi:10.1529/biophysj.105.079483)
7 Engel, G. S., Calhoun, T. R., Read, E. L., Ahn, T. K., Mančal, T., Cheng, Y. C., Blankenship, R. E. & Fleming, G. R. 2007 Evidence for wavelike energy transfer through quantum coherence in photosynthetic systems. *Nature* **446**, 782–786. (doi:10.1038/nature05678)
8 Mohseni, M., Rebentrost, P., Lloyd, S. & Aspuru-Guzik, A. 2008 Environment-assisted quantum walks in photosynthetic energy transfer. *J. Chem. Phys.* **129**, 174106. (doi:10.1063/1.3002335)
9 Caruso, F., Chin, A. W., Datta, A., Huelga, S. F. & Plenio, M. B. 2009 Highly efficient energy excitation transfer in light-harvesting complexes: the fundamental role of noise-assisted transport. *J. Chem. Phys.* **131**, 105105. (doi:10.1063/1.3223548).
10 Ishizaki, A. & Fleming, G. R. 2009 Theoretical examination of quantum coherence in a photosynthetic system at physiological temperature. *Proc. Natl Acad. Sci. USA* **106**, 17 255–17 260. (doi:10.1073/pnas.0908989106)
11 Cheng, Y. C. & Fleming, G. R. 2009 Dynamics of light harvesting in photosynthesis. *Annu. Rev. Phys. Chem.* **60**, 241–262. (doi:10.1146/annurev.physchem.040808.090259)
12 Mukamel, S. 1995 *Principles of nonlinear optical spectroscopy*. Oxford, UK: Oxford University Press.
13 Cheng, Y. C., Engel, G. S. & Fleming, G. R. 2007 Elucidation of population and coherence dynamics using cross-peaks in two-dimensional electronic spectroscopy. *Chem. Phys.* **341**, 285–295. (doi:10.1016/j.chemphys.2007.07.049)
14 Cheng, Y. C. & Fleming, G. R. 2008 Coherence quantum beats in two-dimensional electronic spectroscopy. *J. Phys. Chem. A* **112**, 4254–4260. (doi:10.1021/jp7107889)
15 Plenio, M. B. & Huelga, S. F. 2008 Dephasing-assisted transport: quantum networks and biomolecules. *New J. Phys.* **10**, 113019. (doi:10.1088/1367-2630/10/11/113918).
16 Hayes, D., Panitchayangkoon, G., Fransted, K. A., Caram, J. R., Wen, J., Freed, K. F. & Engel, G. S. 2010 Dynamics of electronic dephasing in the Fenna–Matthews–Olson complex. *New J. Phys.* **12**, 065042. (doi:10.1088/1367-2630/12/6/065042).

17 Hayes, D.& Engel, G. S. 2011 Extracting the excitonic hamiltonian of the Fenna–Matthews–Olson complex using three-dimensional third-order electronic spectroscopy. *Biophys. J.* **100**, 2043–2052. (doi:10.1016/j.bpj.2010.12.3747)
18 Hybl, J. D., Ferro, A. A. & Jonas, D. M. 2001 Two-dimensional Fourier transform electronic spectroscopy. *J. Chem. Phys.* **115**, 6606–6622. (doi:10.1063/1.1398579)
19 Cowan, M. L., Ogilvie, J. P. & Miller, R. J. D. 2004 Two-dimensional spectroscopy using diffractive optics based phased-locked photon echoes. *Chem. Phys. Lett.* **386**, 184–189. (doi:10.1016/j.cplett.2004.01.027)
20 Brixner, T., Mančal, T., Stiopkin, I. V. & Fleming, G. R. 2004 Phase-stabilized two-dimensional electronic spectroscopy. *J. Chem. Phys.* **121**, 4221–4236. (doi:10.1063/1.1776112)
21 Cho, M. H. 2008 Coherent two-dimensional optical spectroscopy. *Chem. Rev.* **108**, 1331–1418. (doi:10.1021/cr078377b)
22 Calhoun, T. R., Ginsberg, N. S., Schlau-Cohen, G. S., Cheng, Y. C., Ballottari, M., Bassi, R. & Fleming, G. R. 2009 Quantum coherence enabled determination of the energy landscape in light-harvesting complex II. *J. Phys. Chem. B.* **113**, 16 291–16 295. (doi:10.1021/jp908300c)
23 Read, E. L., Schlau-Cohen, G. S., Engel, G. S., Wen, J., Blankenship, R. E. & Fleming, G. R. 2008 Visualization of excitonic structure in the Fenna–Matthews–Olson photosynthetic complex by polarization-dependent two-dimensional electronic spectroscopy. *Biophys. J.* **95**, 847–856. (doi:10.1529/biophysj.107.128199)
24 Zheng, J., Kwak, K. & Fayer, M. D. 2007 Ultrafast 2D IR vibrational echo spectroscopy. *Acc. Chem. Res.* **40**, 75–83. (doi:10.1021/ar068010d)
25 Read, E. L., Engel, G. S., Calhoun, T. R., Mančal, T., Ahn, T. K., Blankenship, R. E. & Fleming, G. R. 2007 Cross-peak-specific two-dimensional electronic spectroscopy. *Proc. Natl Acad. Sci. USA* **104**, 14 203–14 208. (doi:10.1073/pnas.0701201104)
26 Demirdöven, N., Khalil, M. & Tokmakoff, A. 2002 Correlated vibrational dynamics revealed by two-dimensional infrared spectroscopy. *Phys. Rev. Lett.* **89**, 237401. (doi:10.1103/PhysRevLett.89.237401)
27 Khalil, M., Demirdöven, N. & Tokmakoff, A. 2003 Coherent 2D IR spectroscopy: molecular structure and dynamics in solution. *J. Phys. Chem. A* **107**, 5258–5279. (doi:10.1021/jp0219247)
28 Pisliakov, A. V., Mančal, T. & Fleming, G. R. 2006 Two-dimensional optical three-pulse photon echo spectroscopy. II. Signatures of coherent electronic motion and exciton population transfer in dimer two-dimensional spectra. *J. Chem. Phys.* **124**, 234 505–234 514. (doi:10.1063/1.2200705)
29 Lee, H., Cheng, Y. C. & Fleming, G. R. 2007 Coherence dynamics in photosynthesis: protein protection of excitonic coherence. *Science* **316**, 1462–1465. (doi:10.1126/science.1142188)
30 Wen, J. Z., Zhang, H., Gross, M. L. & Blankenship, R. E. 2009 Membrane orientation of the FMO antenna protein from *Chlorobaculum tepidum* as determined by mass spectrometry-based footprinting. *Proc. Natl Acad. Sci. USA* **106**, 6134–6139. (doi:10.1073/pnas.0901691106)
31 Lepetit, L., Chériaux, G. & Joffre, M. 1995 Linear techniques of phase measurement by femtosecond spectral interferometry for applications in spectroscopy. *J. Opt. Soc. Am., B, Opt. Phys.* **12**, 2467–2474. (doi:10.1364/JOSAB.12.002467)
32 Stone, K. W., Gundogdu, K., Turner, D. B., Li, X., Cundiff, S. T. & Nelson, K. A. 2009 Two-quantum 2D FT electronic spectroscopy of biexcitons in GaAs quantum wells. *Science* **324**, 1169–1173. (doi:10.1126/science.1170274)
33 Christensson, N., Milota, F., Hauer, J., Sperling, J., Bixner, O., Nemeth, A. & Kauffmann, H. F. 2011 High frequency vibrational modulations in two-dimensional electronic spectra and their resemblance to electronic coherence signatures. *J. Phys. Chem. B* **115**, 5383–5391. (doi:10.1021/jp109442b)
34 Hayes, D., Wen, J., Panitchayangkoon, G., Blankenship, R. E. & Engel, G. S. 2011 Robustness of electronic coherence in the Fenna–Matthews–Olson complex to vibronic and structural modifications. *Faraday Discuss.* **150**, 459–469. (doi:10.1039/C0FD00030B)
35 Turner, D. B., Wilk, K. E., Curmi, P. M. G. & Scholes, G. D. 2011 Comparison of electronic and vibrational coherence measured by two-dimensional electronic spectroscopy. *J. Phys. Chem. Lett.* **2**, 1904–1911. (doi:10.1021/jz200811p)